EARTHARXIV PREPRINT COVERSHEET

Calibrated probabilistic ET0 forecasting with lightweight deep learning across northern and southern Xinjiang: seven-station evaluation and irrigation implications

Dachun Chen1, Chunfang Yue1,*

1 College of Water Conservancy and Civil Engineering, Xinjiang Agricultural University, Urumqi 830000, China

E-mail: Dachun Chen, vision_studio@sina.com; Chunfang Yue, 312172392@qq.com
ORCID: Dachun Chen, 0009-0003-1946-3806
* Corresponding author: Chunfang Yue, vision_studio@sina.com

PREPRINT STATUS

This is a non-peer-reviewed preprint submitted to EarthArXiv. It has not been published in a peer-reviewed journal.

A previous version of this manuscript was submitted to Agriculture (MDPI) for journal peer review and was not accepted for publication. No journal publication DOI is associated with this preprint.

Preprint server: EarthArXiv

Submission date: 9 November 2026

Mastodon handle: not provided.

This coversheet is page 1 of the manuscript. The manuscript begins on page 2.

Calibrated probabilistic ET0 forecasting with lightweight deep learning across northern and southern Xinjiang: seven-station evaluation and irrigation implications

Dachun Chen 1 and Chunfang Yue 1,*

1 College of Water Conservancy and Civil Engineering, Xinjiang Agricultural University, Urumqi 830000, China; vision_studio@sina.com (D.C.); 312172392@qq.com (C.Y.)
* Correspondence: vision_studio@sina.com; ORCID: 0009-0003-1946-3806

Abstract

Accurate and calibrated reference evapotranspiration (ET0) forecasts are essential for irrigation scheduling, yet many ET0 studies report deterministic point forecasts and evaluate only a limited number of forecast origins. This study compared deterministic and probabilistic ET0 forecasts at seven NCEI stations in northern and southern Xinjiang, including Kashi, Hotan, Korla and Turpan as external stations. Daily records from 1 January 1984 to 16 May 2025 were divided chronologically into 70% training, 10% validation and 20% testing. Four model families were evaluated: DLinear, ENMAMBA, CNNBiLSTM and Crossformer. H7, H30 and H180 forecasts were assessed at all feasible test origins using moving-block bootstrap inference and Holm correction. Rolling conformal calibration generated probabilistic forecasts evaluated by dense-grid CRPS, PICP80, PICP90, MPIW80 and MPIW90. A 2024 drip-irrigated cotton record was used to test how forecast strategies interact with actual irrigation deliveries and generic sandy-loam parameters. DLinear achieved the lowest H30 and H180 RMSE in the northern and external station groups. Overall PICP80/PICP90 was close to nominal, but spring and summer intervals remained under-covered. The irrigation simulation did not reproduce observed root-zone moisture; its decision implications are therefore treated as a bounded sensitivity analysis rather than a field-calibrated recommendation.

Keywords: reference evapotranspiration; probabilistic forecasting; DLinear; Mamba; conformal calibration; irrigation scheduling

1. Introduction

Reference evapotranspiration is a core variable in agricultural water management because it links atmospheric demand to crop water use, irrigation requirements and regional water allocation [1]. The FAO-56 Penman-Monteith formulation remains the reference method for calculating ET0, but its application depends on complete meteorological observations and is sensitive to data quality and local climate conditions [2]. In data-scarce regions, machine learning and deep learning models have therefore been used to estimate or forecast ET0 from limited meteorological inputs [3,4].

Recent ET0 forecasting studies have moved from classical regression to recurrent networks, convolutional recurrent models, attention mechanisms and hybrid decomposition methods. Multi-step LSTM and Bi-LSTM models have been used for daily and forward

forecasting [5], while encoder-decoder and optimized deep learning workflows have improved multi-step ET0 prediction [6,7,8]. Hybrid machine learning systems have also been evaluated across climate regions and different input configurations [9,10,11,12]. More recent studies have used improved Informer architectures, AI weather models and attention-enhanced autoencoders [13,14,15]. These studies establish that nonlinear models can capture ET0 dynamics, but their evaluation usually stops at deterministic error metrics.

Irrigation decisions do not depend only on the expected ET0 value. They also depend on the upper tail of future atmospheric demand, because an underestimated high-ET0 period can cause insufficient irrigation and crop water stress. Probabilistic multivariate forecasting has developed rapidly through diffusion models and uncertainty-aware state-space models [16,17]. ET0 products and gridded estimates also contain substantial uncertainty across regions and time scales [18,19]. Despite this progress, probabilistic ET0 forecasting remains less developed than deterministic ET0 prediction, particularly when computational resources and meteorological inputs are limited.

Model complexity is another unresolved issue. Transformer models such as Crossformer and iTransformer can model cross-variable and cross-time dependencies [20,21], and TimeMixer explicitly combines multiscale seasonal and trend components [22]. Mamba and related selective state-space models offer linear-time sequence modeling [23,24], but their practical advantage over simpler models depends on data size, horizon and training budget. DLinear is a low-complexity alternative that decomposes a series into trend and seasonal components and applies linear projections [25]. If DLinear provides similar accuracy and better calibrated uncertainty, it may be preferable for edge-based irrigation systems and stations with limited computing resources.

This study addresses four questions. First, how do lightweight and high-capacity deep learning models compare under a full rolling evaluation across seven stations in northern and southern Xinjiang? Second, does the model ranking remain stable at external South Xinjiang and Turpan sites that are not part of the northern core analysis? Third, can model-agnostic conformal calibration provide reliable probabilistic ET0 forecasts across horizons and seasons without modifying each backbone? Fourth, how do forecast-based irrigation strategies compare with a real 2024 irrigation-delivery record when soil and crop parameters are explicitly treated as generic assumptions? The results are intended to support conditional model selection and data-quality-aware irrigation analysis rather than to claim that one architecture is universally superior.

2. Materials and Methods

2.1. Study area and data

The study used seven NCEI stations. Altay, Urumqi and Jinghe formed the northern core, and Kashi, Hotan and Korla formed an external South Xinjiang group. Turpan was retained as an additional arid low-elevation contrast. The seven stations span elevations from 39.3 m at Turpan to 1,380.4 m at Kashi and represent northern mountain-fringe, basin, oasis and depression environments. Station metadata and roles are summarized in Table 1. Daily records covered 1984-01-01 to 2025-05-16, giving 15,112 calendar days per station.

Table 1. Station network, role and elevation.

Station	Role	Latitude	Longitude	Elevation (m)
Altay	North core	47.7333	88.0833	737.0
Urumqi	North core	43.7833	87.6167	919.0
Jinghe	North core	44.5667	82.8167	330.2

Station	Role	Latitude	Longitude	Elevation (m)
Kashi	External south	39.5429	76.0200	1380.4
Hotan	External south	37.1333	79.9333	1375.0
Korla	External south	41.7333	85.8167	903.0
Turpan	Arid contrast	42.9500	89.2297	39.3

Maximum temperature, minimum temperature, dew-point temperature, precipitation and wind speed were extracted from NCEI GSOD station archives. Temperature variables were converted from Fahrenheit to Celsius. Wind speed was converted from knots to metres per second and then adjusted from 10 m to 2 m following the FAO-56 logarithmic relation [1]. Station-specific NASA POWER daily files provided all-sky surface shortwave downward irradiance in MJ m-2 day-1. The POWER header identifies the source product as CERES SYN1deg. These radiation data are not the MERRA2 M2T1NXRAD product, and this distinction is maintained throughout the study. POWER precipitation was available for the four external stations and was compared with NCEI precipitation. The three northern POWER files did not contain PRECTOTCORR, so independent precipitation validation for those stations remains incomplete.

2.2. FAO-56 ET0 calculation and quality control

The target variable was daily ET0 calculated with the FAO-56 Penman-Monteith equation. FAO Irrigation and Drainage Paper 56 remains the reference formulation for daily reference evapotranspiration [1]. The equation combines an energy-balance term and an aerodynamic term:

$$ET_0 = \frac{0.408\Delta(R_n - G) + \gamma \frac{900}{T + 273} u_2 (e_s - e_a)}{\Delta + \gamma(1 + 0.34u_2)} \quad (1)$$

where ET0 is reference evapotranspiration (mm day-1), Rn is net radiation at the crop surface (MJ m-2 day-1), G is soil heat flux (MJ m-2 day-1), Tmean is mean daily air temperature (°C), u2 is wind speed at 2 m (m s-1), es is saturation vapour pressure (kPa), ea is actual vapour pressure (kPa), Δ is the slope of the saturation vapour pressure curve (kPa °C-1), and γ is the psychrometric constant (kPa °C-1).

Mean daily temperature was calculated as Tmean = (Tmax + Tmin) / 2. Saturation vapour pressure was calculated from Tmax and Tmin:

$$e_s = \frac{e_0(T_{max}) + e_0(T_{min})}{2}, e_0(T) = 0.6108 \exp\left(\frac{17.27T}{T + 237.3}\right) \quad (2)$$

Actual vapour pressure was derived from dew-point temperature:

$$e_a = 0.6108 \exp\left(\frac{17.27T_{dew}}{T_{dew} + 237.3}\right) \quad (3)$$

Mean relative humidity was derived as RHmean = 100 ea / es and constrained to the physical range 0-100% for the model inputs. Atmospheric pressure was adjusted for station elevation, and the psychrometric constant was calculated from the adjusted pressure. Extraterrestrial radiation Ra was calculated from latitude, solar declination and sunset hour angle. Clear-sky radiation was estimated as Rso = (0.75 + 2 × 10-5 z) Ra, where z is elevation in metres. Net shortwave radiation was calculated as Rns = (1 - α) Rs with an albedo α of 0.23. Net longwave radiation followed the FAO-56 formulation, and net radiation was calculated as Rn = Rns - Rnl. Daily soil heat flux was set to zero following the standard daily calculation.

All station files were checked for duplicate dates, missing calendar days, missing or non-finite values, physically implausible ranges and NCEI flags. Missing calendar-day fractions ranged from 0.106% at Kashi to 0.496% at Jinghe. Wind and relative-humidity

anomalies were compared with monthly model error, but no single breakpoint explained the ranking across all stations. The forecasting feature set was Tmax, Tmin, RHmean, u(x), Rs and ET0. Each station was trained and evaluated independently, and the external stations did not participate in the northern calibration or model-selection steps.

2.3. Chronological split and preprocessing

Each station was divided chronologically into 70% training, 10% validation and 20% testing. No future information was used in scaling, calibration or model selection. Training statistics were used for standardization. The feature matrix at time t was defined as Xt = [Tmax, Tmin, RHmean, u2, Rs] and the forecasting target was ET0. For a lookback window L and forecast horizon H, each model learned a mapping from X(t-L+1:t) to ET0(t+1:t+H). The same lookback and forecast origins were applied across models.

All feasible rolling origins in the final 20% test partition were used. The first test origin was 2017-02-05. H7, H30 and H180 had 3,017, 2,994 and 2,844 origins, respectively, after removing origins whose targets extended beyond the available record. The training, validation and test boundaries were identical for all models and seeds. This design prevents information leakage from the test period into scaling, calibration or model selection.

2.4. Forecasting models

2.4.1. DLinear

DLinear was included as the low-complexity linear benchmark [25]. The model first decomposes the input sequence into trend and seasonal components by moving average:

$$X_{trend} = MovingAverage(X) \quad (4)$$

$$X_{seasonal} = X - X_{trend} \quad (5)$$

The two components are projected to the forecast horizon by separate linear layers:

$$Y = W_{trend}X_{trend} + W_{seasonal}X_{seasonal} \quad (6)$$

The moving-average kernel controls the temporal scale of the trend component. The main experiment used a kernel of 181 days. The 31-day and 365-day kernels were evaluated in the decomposition ablation. DLinear has few parameters, does not use recurrent state, and provides a transparent baseline for comparing accuracy against computational cost.

2.4.2. ENMAMBA

ENMAMBA combines seasonal-trend decomposition with a selective state-space encoder [23,24]. The input series is decomposed into trend and seasonal components by a moving-average filter. Each component is independently normalized and passed through inverted data embedding. The trend branch and seasonal branch use separate Mamba encoders. A selective state-space model updates a latent state through input-dependent transitions:

$$h_t = A_t\, h_{t-1} + B_t\, x_t \quad (7)$$

$$y_t = C_t\, h_t \quad (8)$$

where At, Bt and Ct depend on the input, allowing the model to retain or forget information according to the current sequence. The trend and seasonal outputs are projected separately to the forecast horizon and then summed. In this study, the principal ENMAMBA configuration used d_model = 32, d_state = 16, two encoder layers, a moving-average kernel of 181 days, a feed-forward width of 256 and one expert. State dimensions of 16, 32 and 64 were evaluated in the ablation experiment.

2.4.3. CNNBiLSTM

CNNBiLSTM combines convolutional feature extraction and bidirectional recurrent modeling. A one-dimensional convolution is first applied along the time axis to capture

passed to a bidirectional LSTM. The forward LSTM processes the sequence from the past to the future, while the backward LSTM processes the reversed sequence:

$$h_t^f = LSTM_f(x_t, h_{t-1}^f) \quad (9)$$

$$h_t^b = LSTM_B(x_t, h_{t+1}^b) \quad (10)$$

$$h_t = [h_t^f, h_t^b] \quad (11)$$

The concatenated hidden state is passed through dropout and a linear prediction head. In the mixed-variable configuration, the convolution receives all meteorological variables jointly, so the model can learn interactions among temperature, humidity, radiation and wind speed. In the channel-independent configuration, each variable is processed separately and the interaction information is removed. The main model used a CNN width of 128, a convolutional kernel of 3, one BiLSTM layer, a hidden size equal to the CNN width and a dropout rate of 0.1.

2.4.4. Crossformer

Crossformer was included as a high-capacity attention benchmark [20]. The input is divided into temporal segments, embedded into a d_model space and processed by a two-stage attention encoder. The first stage applies attention across time steps within the same variable. The second stage applies attention across variables. This design allows Crossformer to represent both temporal dependence and cross-variable dependence. The decoder uses a learnable query representation, cross-attention on the encoder output and a projection head. The main experiment used d_model = 128, d_ff = 256, two encoder layers and eight attention heads. Crossformer therefore serves as an upper-bound model for cross-time and cross-variable representation, but it also provides a direct test of whether a much larger model yields operational gains.

2.4.5. Supplementary architectures

The supplementary comparison included iTransformer, TimeMixer, xPatch, PatchTST and MTGNN. iTransformer inverts the attention dimension and models relationships among variables [21]. TimeMixer combines multiscale seasonal and trend mixing [22]. xPatch uses dual-stream seasonal-trend decomposition with patching [26]. PatchTST treats subseries as tokens [27]. MTGNN represents variable relations with a graph neural network [28]. These architectures were used for structural ablation and benchmark context rather than as the primary operational candidates.

2.4.6. Training configuration

All neural models used an input window of 730 days, a batch size of 64, Adam optimization and an initial learning rate of 10-4. The main experiment used five epochs, patience 3 and all feasible rolling origins. The complete seed-2021 matrix contained 84 runs, representing four models, seven stations and three horizons. H30 was repeated with seeds 2022 and 2023 to test initialization stability, adding 56 runs with no failures. A training-budget check at Kashi H30 compared 5, 15 and 30 epochs for the four models. The main hyperparameters are summarized in Table 2.

Table 2. Main model mechanisms and architecture-specific settings.

Model	Mechanism	Key settings	Role
DLinear	Moving-average decomposition and linear projection	moving_avg=181 / seq_len=730	Low-complexity benchmark
ENMAMBA	Separate trend and seasonal Mamba branches	d_model=32 / d_state=16 / e_layers=2	Lightweight state-space model

Model	Mechanism	Key settings	Role
CNNBiLSTM	CNN feature extraction and mixed-variable BiLSTM	d_model=128 / kernel=3 / BiLSTM=1	Variable-interaction model
Crossformer	Two-stage cross-time and cross-variable attention	d_model=128 / d_ff=256 / heads=8 / layers=2	High-capacity benchmark

2.5. Probabilistic post-processing and conformal calibration

For each model, horizon and seed, validation-period predictions were reconstructed from the saved model checkpoint. Residuals were defined as r = ET0,obs - ET0,pred. Seven residual quantiles were estimated: 0.05, 0.10, 0.25, 0.50, 0.75, 0.90 and 0.95. These quantiles were added to deterministic test predictions to form seven predictive quantiles:

$$q_\tau(test) = ET_{0,median}(test) + q_\tau(residual) \quad (12)$$

Quantile crossing was removed by sorting the predicted quantiles at each lead time. Four calibration paths were compared: raw validation quantiles, a fixed validation split, a seasonal split and a rolling validation pool. The rolling pool began with validation residuals and expanded as test origins advanced. Conformal offsets were applied separately to the 80% and 90% intervals and evaluated by lead time and season:

$$L_I = q_{\alpha/2}(test) - c_{1-\alpha} \quad (13)$$

$$U_I = q_{1-\alpha/2}(test) + c_{1-\alpha} \quad (14)$$

where LI and UI are the calibrated lower and upper bounds and c1-α is the finite-sample conformal offset estimated from calibration nonconformity scores. The absolute residual score was used for symmetric intervals. The primary probability metrics were dense-grid CRPS, Pinball loss, PICP80, PICP90, MPIW80 and MPIW90. Dense-grid CRPS was used because the seven-quantile approximation differed by roughly 9-16%. Conformal calibration was used as a model-agnostic layer so that probabilistic comparison did not depend on a model-specific output head [16,17].

2.6. Irrigation decision experiment

A simplified daily root-zone water balance was used to convert ET0 forecasts into irrigation decisions. The field validation used a 2024 drip-irrigated cotton site at 44.5625 N, 82.2280556 E on sandy loam. The reported irrigation season ended on 2024-09-10. The actual delivery record contained 23 cotton-water-user events, 137.268 x 10^4 m3 of delivered water and a command area of 0.5907 x 10^4 mu, corresponding to a seasonal depth of 348.6 mm. Soil moisture was monitored at 20, 30 and 40 cm from 2024-05-24 to 2024-09-23. The 10 cm record was excluded because it did not pass physical-range screening.

The simulated root-zone parameters were regional generic assumptions for drip-irrigated cotton on sandy loam rather than field-calibrated measurements. The root depth ranged from 0.25 to 0.80 m, field capacity from 0.24 to 0.30 m3 m-3, wilting point from 0.08 to 0.12 m3 m-3, management-allowed depletion from 0.55 to 0.70 of total available water, event depth from 10 to 30 mm, minimum interval from one to three days and application efficiency from 0.85 to 0.95.

Seven scheduling strategies were compared: deterministic median, probability mean, Q75, Q90, Q95, a fixed seven-day schedule and a perfect-forecast reference. The perfect-forecast reference used realized future ET0 under the same event-depth and interval constraints; it is not a globally optimal controller. The reported real delivery schedule was evaluated as an additional benchmark. Forecast-based scenarios were tested under both zero-rain and observed-rain information settings, and one-at-a-time sensitivity analyses covered soil water limits, root depth, management-allowed depletion, event depth, minimum interval, irrigation efficiency and cost.

The decision metrics were cumulative irrigation, irrigation events, deficit days, mean

decision regret. The decision experiment follows prior work on irrigation scheduling with imperfect weather forecasts and soil-water models [29,30,31,32,33], and it adopts the FAO56 soil-water balance perspective [34].

2.7. Ablation and transfer experiments

Five ablation groups were evaluated. The decomposition group compared moving-average scales of 31, 181 and 365 days and different seasonal-trend decompositions. The probability group compared a DLinear model with an internal quantile head against deterministic DLinear with external conformal calibration. The variable-mixing group compared channel-independent and mixed-variable CNNBiLSTM. The state group compared different Mamba state dimensions. The transfer group evaluated zero-shot forecasting from one station to another using the same feature set.

2.8. Metrics and statistical analysis

Deterministic performance was assessed with RMSE, MAE, NSE and KGE. Probabilistic performance was assessed with dense-grid CRPS, Pinball loss, PICP and MPIW. Computational efficiency was assessed with training time, inference time and parameter count. The main rolling matrix used seed 2021, and H30 initialization stability used seeds 2021, 2022 and 2023.

Paired model and baseline comparisons used moving-block bootstrap on rolling-origin error blocks. The block length equaled the forecast horizon, 2,000 bootstrap replicates were used, and Holm correction was applied within each station and horizon. RMSE, MAE, CRPS, PICP and MPIW were reported with confidence intervals. Random-seed variation was used only to describe initialization stability and was not treated as independent temporal replication. The strongest simple benchmark was the 15-day smoothed seasonal climatology estimated from training data only.

3. Results

3.1. Study domain and data completeness

The expanded evaluation covers seven stations and 15,112 days per station. The northern core contains Altay, Urumqi and Jinghe, while Kashi, Hotan and Korla represent the South Xinjiang oasis and Tarim Basin settings, and Turpan provides an arid depression contrast. Missing calendar-day fractions remain below 0.5% at every station. The same 70/10/20 split was used for all sites, and the first rolling origin was 2017-02-05. H7, H30 and H180 contain 3,017, 2,994 and 2,844 feasible origins, respectively. Table 1 summarizes the station network and Figure 1 shows the original data and evaluation design.

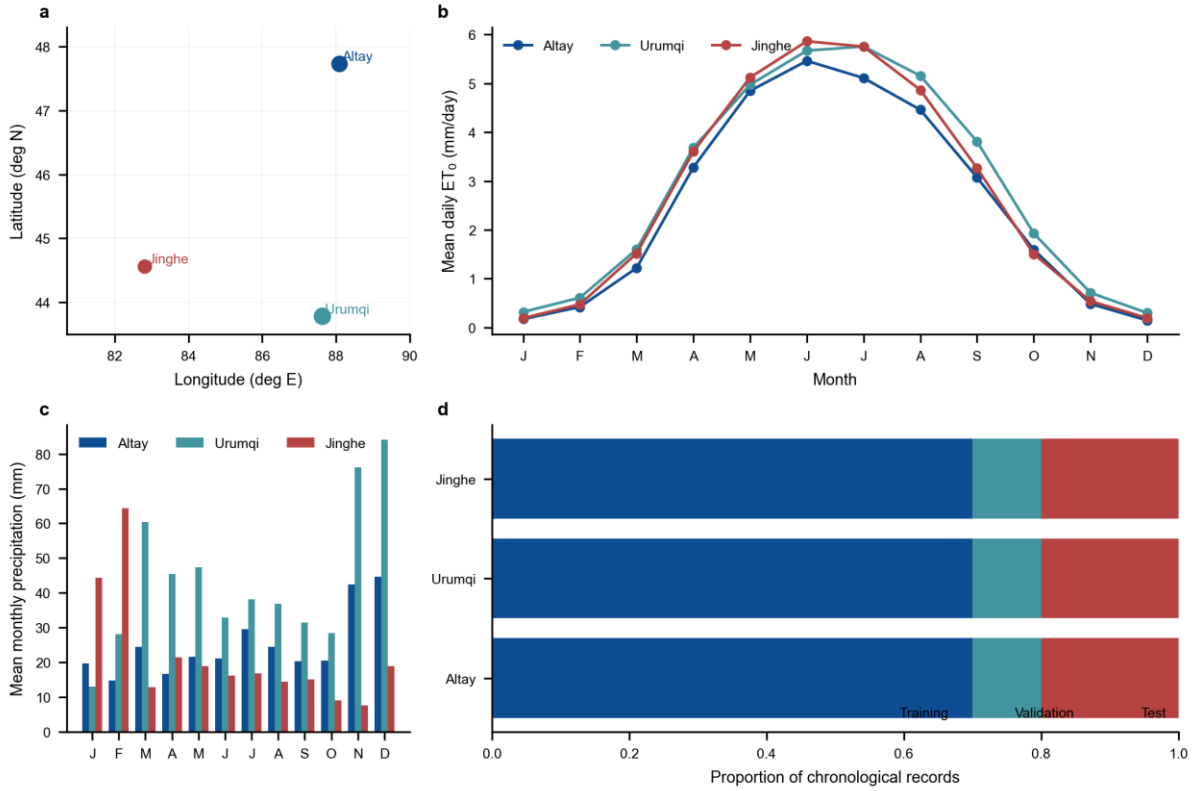


Figure 1. Core data and evaluation protocol. Monthly ET0 and precipitation, station locations and the common chronological training, validation and test split for the original northern core. The external South Xinjiang and Turpan evaluation is shown in Figure 6.

3.2. Deterministic performance under complete rolling evaluation

The full rolling evaluation changes the earlier station ranking. In the northern group, DLinear had the lowest mean RMSE at H7 (0.8274 mm/day), H30 (0.8471 mm/day) and H180 (0.8476 mm/day). In the external group, CNNBiLSTM had a small H7 advantage (0.8797 mm/day versus 0.8851 mm/day for DLinear), but DLinear was best at H30 (0.9033 mm/day) and H180 (0.9078 mm/day). The next non-DLinear external H30 result was 0.9164 mm/day for CNNBiLSTM, and Crossformer reached 0.9415 mm/day. Regional RMSE is summarized in Table 3.

Table 3. Regional rolling RMSE for DLinear and the best non-DLinear model.

Region	Horizon	DLinear RMSE	Best non-DLinear	Best non-DLinear RMSE	Difference (%)
External	H180	0.9078	CNNBiLSTM	0.9271	2.12
External	H30	0.9033	CNNBiLSTM	0.9164	1.45
External	H7	0.8851	CNNBiLSTM	0.8797	-0.61
Northern	H180	0.8476	CNNBiLSTM	0.8547	0.84
Northern	H30	0.8471	Crossformer	0.851	0.46
Northern	H7	0.8274	ENMAMBA	0.8368	1.14

The external stations are systematically harder than the northern core. DLinear RMSE increases by 6.6-7.1% depending on horizon. The result supports a regional transfer boundary: the H7 winner depends on the station group, while the H30 and H180 results

favor DLinear in both groups. Crossformer does not retain a consistent advantage outside the northern stations.

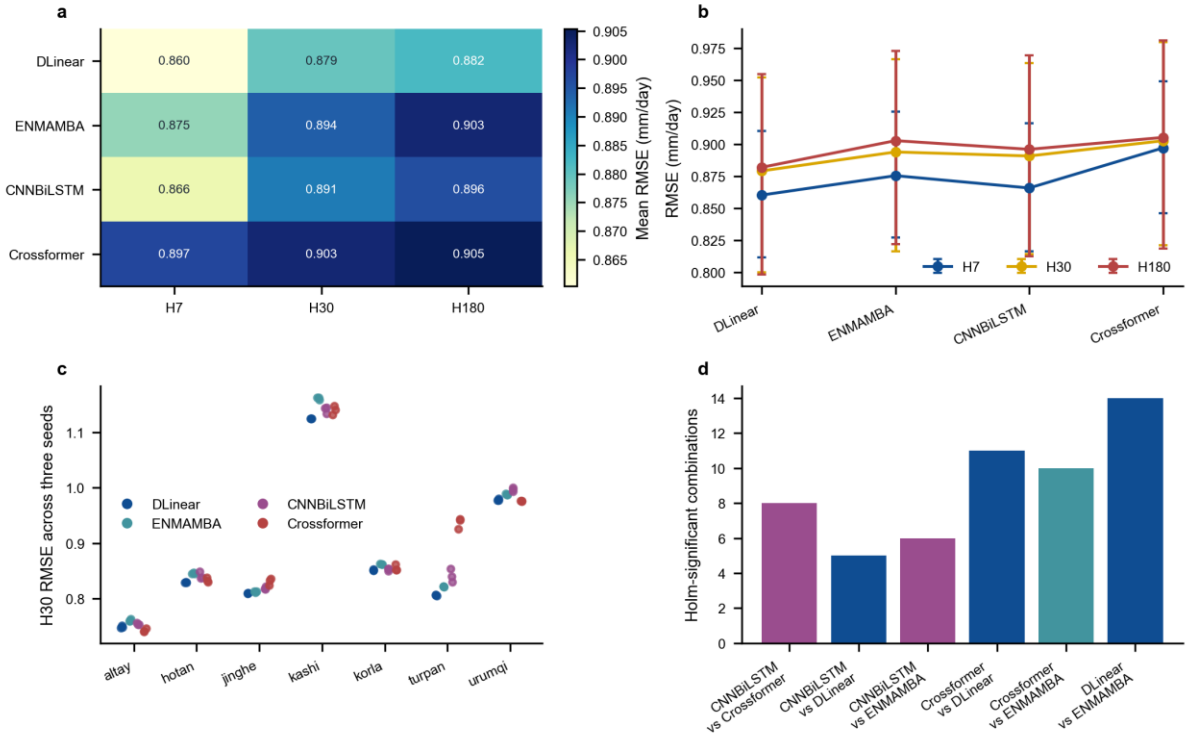


Figure 2. Full rolling deterministic model comparison. Panels show mean RMSE, rolling-origin confidence intervals, H30 seed stability and Holm-significant model comparisons across the seven stations.

3.3. Statistical inference and initialization stability

Moving-block bootstrap comparisons with Holm correction show that DLinear outperformed persistence and the training mean in all 21 station-horizon combinations, and outperformed the seasonal climatology in 15 of 21 combinations. Seasonal climatology remains the strongest simple benchmark. DLinear is never the significantly inferior model in any Holm-significant pairwise comparison.

H30 initialization stability is station-dependent. Across seven stations and three seeds, DLinear is best in 13 of 21 station-seed combinations, Crossformer in 7 and CNNBiLSTM in 1. Crossformer is best at Altay and Urumqi in all three seeds, whereas DLinear is consistently best at Hotan, Jinghe, Kashi and Turpan. The seed analysis supports local initialization stability without treating seeds as independent temporal replicates. The training-budget check at Kashi H30 produced RMSE changes of 0.10%, 0.97%, less than 0.01% and 0.15% for DLinear, ENMAMBA, CNNBiLSTM and Crossformer when comparing 5 and 15 epochs. No model shows systematic underfitting under the main 5-epoch budget.

3.4. Probabilistic calibration and conditional coverage

Rolling conformal calibration has the best overall probability performance among the compared calibration paths. Its mean PICP80/PICP90 is 0.816/0.908 at H7, 0.815/0.907 at H30 and 0.816/0.908 at H180. Dense-grid CRPS is lower than the seven-quantile approximation, with differences of about 9-16%. The denser score is therefore used for the revised probabilistic comparison, and the earlier seven-quantile CRPS is retained only as an approximation. Table 4 summarizes the rolling deterministic and probabilistic performance

Table 4. Rolling deterministic and probabilistic performance across models and forecast horizons.

Model	Horizon	RMSE (mm/day)	CRPS (mm/day)	Grid CRPS delta (%)	PICP80	PICP90	MPIW80 (mm/day)	MPIW90 (mm/day)	Coverage status (P/PA/F)
DLinear	H7	0.8604	0.4302	15.52	0.803	0.903	1.83	2.67	0/0/7
DLinear	H30	0.8792	0.4404	15.67	0.805	0.903	1.89	2.74	0/1/6
DLinear	H180	0.882	0.4437	15.45	0.803	0.902	1.9	2.76	1/6/0
ENMAMBA	H7	0.8755	0.4376	15.68	0.802	0.902	1.85	2.68	0/0/7
ENMAMBA	H30	0.894	0.4501	15.88	0.805	0.904	1.93	2.78	0/2/5
ENMAMBA	H180	0.9028	0.4565	16.08	0.803	0.902	1.97	2.81	2/5/0
CNNBiLSTM	H7	0.8659	0.4638	14.51	0.846	0.925	2.51	3.34	0/0/7
CNNBiLSTM	H30	0.8909	0.4799	14.75	0.845	0.924	2.57	3.43	0/1/6
CNNBiLSTM	H180	0.8961	0.4892	14.81	0.842	0.922	2.63	3.51	0/6/1
Crossformer	H7	0.8972	0.5133	15.91	0.812	0.901	2.42	3.23	1/1/5
Crossformer	H30	0.9027	0.4937	15.88	0.807	0.899	2.24	3.07	1/2/4
Crossformer	H180	0.9053	0.5048	15.96	0.817	0.907	2.43	3.29	2/5/0

Figure 3 shows the reliability, lead-time and seasonal coverage diagnostics. Overall coverage does not imply conditional coverage. PICP80 is approximately 0.68-0.72 in spring and summer at H7 and H30, while winter and autumn approach or exceed nominal coverage. For DLinear under rolling calibration, all seven H7 stations fail the joint criterion and six of seven H30 stations fail, with one partial result. H180 is less severe, with one pass and six partial results. Across all models, the H7 assessment contains 26 failures, one partial result and one pass; H30 contains 21 failures, six partial results and one pass; H180 contains one failure, 22 partial results and five passes. The calibration layer improves average probabilistic scores but does not remove seasonal or site-specific undercoverage.

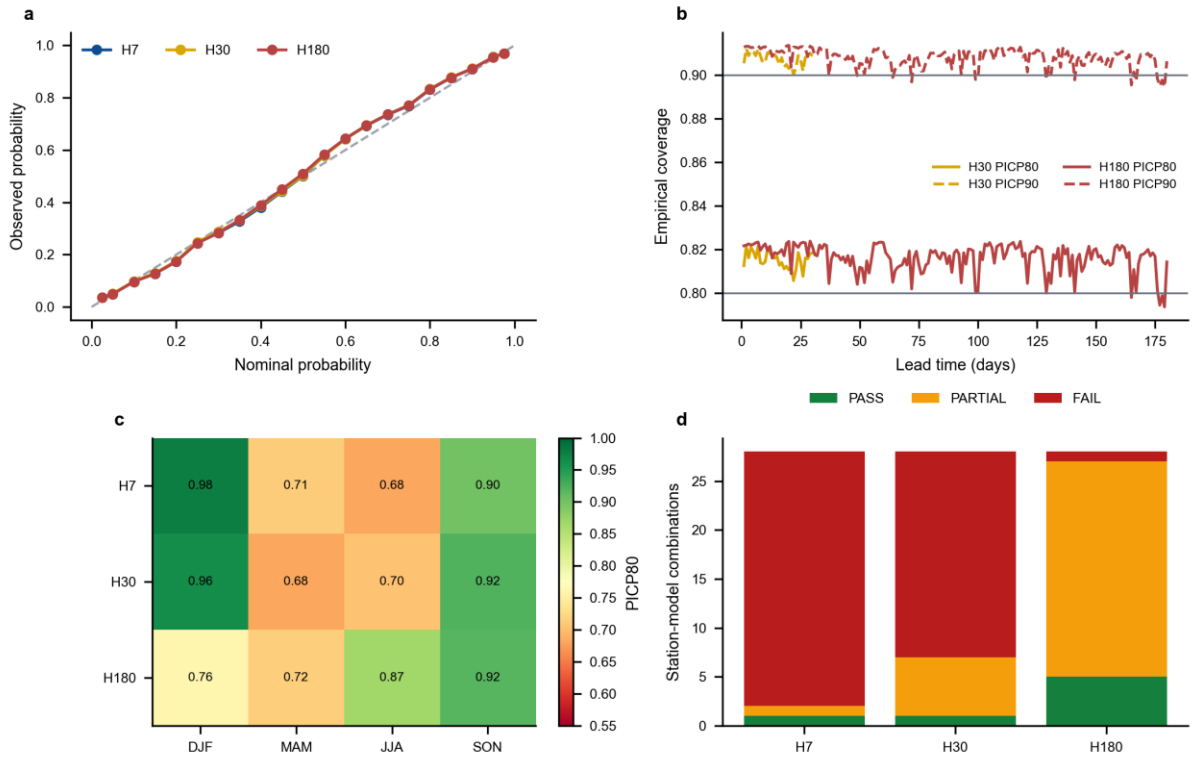


Figure 3. Probabilistic calibration and conditional coverage. Panels show reliability, lead-time coverage, seasonal PICP80 and the PASS/PARTIAL/FAIL assessment after joint overall, lead-time and seasonal criteria.

3.5. Accuracy and computational efficiency

DLinear and ENMAMBA occupy the low-cost region of the accuracy-efficiency space. DLinear requires about 123-147 s per run across horizons, ENMAMBA about 163-179 s, CNNBiLSTM about 252-268 s and Crossformer about 280-369 s. Parameter counts range from 10,234 to 263,160 for DLinear, 104,334 to 115,752 for ENMAMBA, 814,518 to 1,347,012 for CNNBiLSTM and 2,109,970 to 2,142,226 for Crossformer. Inference latency is 4.1-5.2 ms for DLinear, 8.9-10.1 ms for ENMAMBA, 15.6-16.9 ms for CNNBiLSTM and 20.6-21.8 ms for Crossformer. Peak GPU memory remains below 10 MB for DLinear and ENMAMBA but reaches about 43-45 MB for CNNBiLSTM and 28 MB for Crossformer.

The additional capacity of Crossformer does not produce a consistent gain. Under the full rolling protocol, DLinear has the best regional RMSE at H30 and H180 and the lowest dense-grid CRPS in both northern and external groups. Its value therefore lies in the combination of accuracy, probabilistic quality and low inference cost.

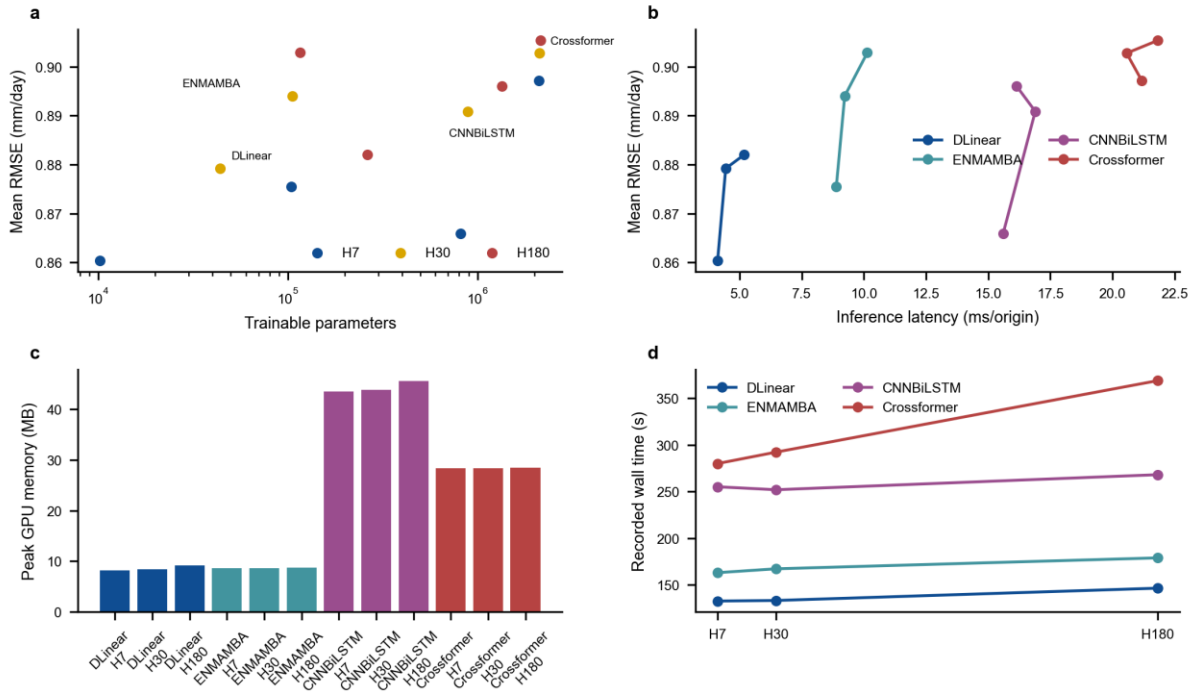


Figure 4. Accuracy, inference cost and parameter count. Panels show trainable parameters, measured GPU inference latency, peak allocated GPU memory and recorded training wall time.

Table 5 reports the corresponding parameter counts, training wall times, inference latency and peak GPU memory.

Table 5. Parameters, training wall time, inference latency and peak GPU memory.

Model	Horizon	Parameters	Training wall time (s)	Inference latency (ms/origin)	Peak GPU memory (MB)
DLinear	H7	10234	132.8	4.12	8.26
DLinear	H30	43860	133.4	4.44	8.39
DLinear	H180	263160	146.6	5.19	9.23
ENMAMBA	H7	104334	163.2	8.89	8.68
ENMAMBA	H30	105852	167.3	9.23	8.69
ENMAMBA	H180	115752	179.1	10.14	8.74
CNNBiLSTM	H7	814518	255.2	15.6	43.44
CNNBiLSTM	H30	885312	252.0	16.9	43.71
CNNBiLSTM	H180	1347012	268.2	16.14	45.47
Crossformer	H7	2109970	280.1	21.18	28.27
Crossformer	H30	2113426	292.3	20.57	28.29
Crossformer	H180	2142226	368.9	21.82	28.4

3.6. Irrigation reconstruction using a real 2024 delivery record

The field record contains 23 cotton delivery events and a seasonal applied depth of 348.6 mm over the reported command area. The simulation with generic sandy-loam and cotton parameters produces different behavior. Deterministic median and probability-mean strategies apply about 605.8 mm, Q90 applies 613.6 mm and Q95 applies 620.4 mm.

The fixed seven-day schedule applies 420 mm. The reported schedule applies substantially less water but yields the largest modeled stress, whereas the forecast-based strategies reduce modeled stress under the nominal parameter set.

This comparison is constrained by parameter uncertainty. The simulated 20-40 cm moisture under the reported schedule has RMSE 0.0531 m3 m-3, MAE 0.0436 m3 m-3, bias -0.0248 m3 m-3 and correlation 0.300 with observations. The generic simulation therefore does not reproduce field water dynamics well enough to support a field-calibrated irrigation recommendation. Sensitivity results show that small event depth, dry soil, low management-allowed depletion, shallow roots and low application efficiency increase stress and can change strategy ranking. The reported schedule remains a real operational benchmark, but the model comparison is a bounded scenario analysis.

Table 6 reports the simulated strategy outcomes, and Figure 5 shows the field comparison and parameter sensitivity.

Table 6. 2024 irrigation strategy comparison under generic sandy-loam and cotton parameters.

Strategy	Irrigation (mm)	Deficit days	Stress index	Deep percolation (mm)	Cost (CNY/ha)
risk_q95	620.4167	1.3667	0.0006	23.9908	4963.3333
risk_q90	613.5833	2.0375	0.0012	18.5917	4908.6667
risk_q75	606.8333	3.0875	0.0022	14.0809	4854.6667
perfect_forecast_reference	608.3333	3.625	0.003	14.0678	4866.6667
probability_mean	605.8333	3.9167	0.0032	12.7201	4846.6667
deterministic_median	605.8333	3.9333	0.0032	12.8371	4846.6667
fixed_7day	420.0	76.6667	0.2931	59.2343	3360.0
actual_reported	348.5729	96.0	0.4022	0.0	2788.583

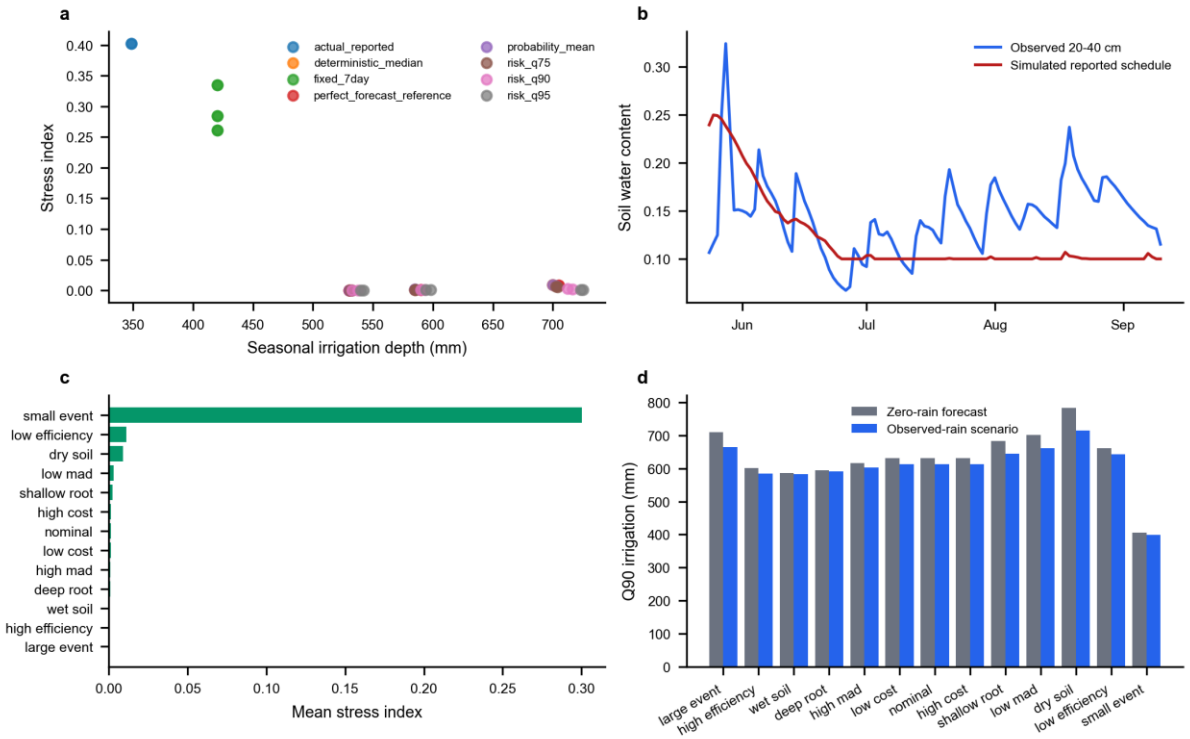


Figure 5. Irrigation reconstruction and parameter sensitivity. Panels show the irrigation-stress trade-off, 2024 observed and simulated soil water, one-at-a-time Q90 sensitivity and zero-rain versus observed-rain information scenarios.

3.7. Ablation results

The structural ablations are retained as supplementary context and are not used to support the main model-selection claims. They examine variable mixing, decomposition scale and state dimension on a smaller evaluation matrix. Their results are useful for model diagnosis, but they do not replace the complete seven-station rolling comparisons or the time-block inference reported above.

3.8. Cross-station transfer

The earlier northern three-station zero-shot transfer experiment is treated as exploratory supplementary evidence, not as the external validation for this paper. External validity is assessed by training and rolling evaluation at each of the seven stations. For a new site without local training data, fine-tuning or a formal transfer test with target-specific calibration is required before deployment.

3.9. External stations and data quality

All four external stations were evaluated at every horizon, not only at H30. The external-station RMSE for DLinear was 0.8851, 0.9033 and 0.9078 mm/day at H7, H30 and H180, respectively. These values are 6.6-7.1% higher than the corresponding northern-core results. CNNBiLSTM was slightly better at H7, but DLinear was best at H30 and H180. Crossformer reached 0.9350-0.9431 mm/day in the external group, so its cross-variable attention did not provide a consistent transfer advantage. Figure 6 summarizes the station-quality and external-validation diagnostics.

POWER and NCEI precipitation were comparable in wet-day occurrence but not in daily amount. Pearson correlations were 0.474 at Kashi, 0.441 at Hotan, 0.304 at Korla and 0.076 at Turpan; daily MAE was 0.149-0.366 mm/day and wet-day agreement was 94.9-98.0%. NCEI missing calendar days ranged from 0.106% to 0.496%. Wind and humidity anomalies had weak to moderate correlations with H7 error, and breakpoint years rarely coincided across stations. Station-to-grid elevation differences were small at Altay and Korla but large at Jinghe (-828.7 m), Turpan (-698.1 m), Hotan (-264.4 m) and Urumqi (+181.7 m). MERRA2 M2T1NXRAD files were not available for the revision, so the independent radiation sensitivity comparison remains unresolved.

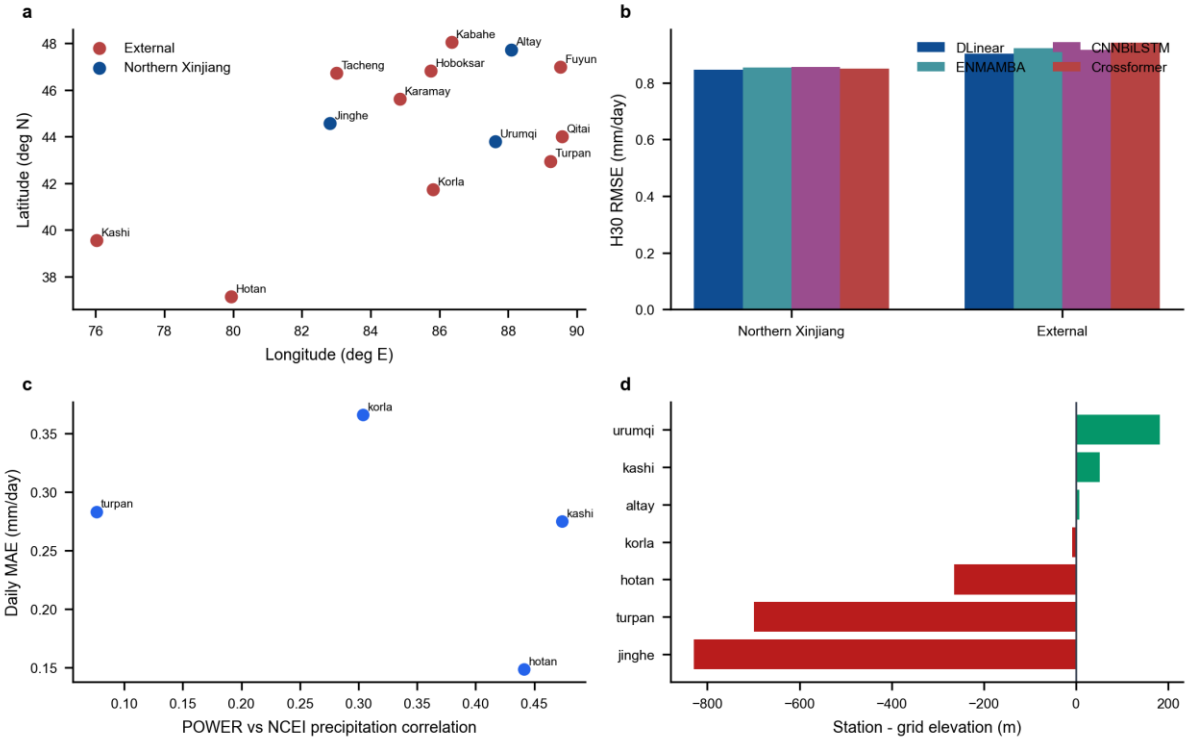


Figure 6. External validation and data quality. Panels show the seven-station domain, H30 model RMSE in northern and external stations, POWER-NCEI precipitation agreement and station-to-grid elevation differences.

4. Discussion

4.1. Model selection depends on horizon

The full rolling evaluation does not support a universal single-model conclusion. DLinear had the best regional RMSE at H30 and H180 in both northern and external groups and the lowest dense-grid CRPS under rolling calibration. H7 is region-dependent: DLinear was best in the northern core, whereas CNNBiLSTM had a small average advantage in the external group. The station-level H30 seed analysis adds another qualification: DLinear was best in 13 of 21 station-seed combinations, but Crossformer was consistently best at Altay and Urumqi. Model ranking therefore depends on station, horizon and initialization as well as the evaluation protocol.

The external-station results matter for operational interpretation. Error increases in the South Xinjiang and Turpan group, and the H7 ranking is not preserved. A single northern-core ranking should not be used to select a model for a new oasis or depression station. Local evaluation, or at least regional validation, is required before deployment.

4.2. Efficiency is a substantive model property

DLinear used roughly one-sixth to one-third of the training time required by Crossformer, depending on horizon and concurrency. In an operational setting, this difference affects retraining frequency, local deployment and the feasibility of running multiple ensemble members. The DLinear results align with the original argument that a simple linear decomposition can be competitive with transformer architectures in time-series forecasting [25].

The result should not be interpreted as evidence that linearity is always sufficient. DLinear was not uniformly best in point accuracy. Its value lies in the combination of accuracy, calibrated uncertainty and resource use. This trade-off is particularly relevant

for irrigation districts and edge systems that cannot maintain a large GPU training environment.

4.3. Calibration changes the interpretation of model performance

Rolling conformal calibration had the best average performance among the compared calibration paths. At H7, H30 and H180, its dense-grid CRPS was about 0.46-0.47, compared with about 0.65-0.70 for the fixed validation split and raw validation quantiles. The seasonal split produced narrower intervals but much worse coverage. Rolling calibration therefore provided the most defensible common probability layer across models, while still exposing conditional undercoverage [16,17].

Calibration did not solve all uncertainty problems. Rolling calibration matched overall PICP closely, but spring and summer PICP80 remained near 0.68-0.72, and H7/H30 failed the joint coverage criterion at most stations. The discrepancy indicates conditional distribution shift, not only insufficient calibration-pool size. Seasonal and regime-aware calibration should be tested, and operational use should report coverage by season and lead time rather than a single overall PICP.

4.4. Decision value is site-specific

The 2024 field reconstruction shows why irrigation evidence must remain parameter-aware. Forecast-based strategies apply roughly 606-620 mm under the nominal generic parameter set, whereas the real delivery record applies 348.6 mm. The difference is large, and the simulated soil moisture does not reproduce the 20-40 cm observations well (correlation 0.300). The discrepancy can reflect generic soil and crop parameters, differences between command-area deliveries and plot-level application, and the distance between the field and the Jinghe weather station.

These results do not establish a field-calibrated irrigation benefit. They show that strategy comparisons are sensitive to event depth, root depth, management-allowed depletion, soil texture and application efficiency. The reported schedule is a valid operational benchmark, but the forecast strategies remain scenario-based. Field-specific FC, WP, root-zone depth, rainfall, crop coefficients and yield or cost data are needed before operational recommendations can be made [29,30,33].

4.5. Limitations

Several limitations remain. Seven stations broaden the domain within Xinjiang, but all are still in one broad arid and semi-arid region, so this is not a cross-continental external validation. The radiation data are POWER/CERES daily values and should not be described as MERRA2 M2T1NXRAD radiation. MERRA2 sensitivity remains pending. Northern POWER files lack precipitation, so precipitation validation is complete only for the external stations. The field simulation uses generic sandy-loam and cotton parameters and does not reproduce observed root-zone moisture; runoff, capillary rise, crop-specific root growth and farmer behaviour are not represented. Long-horizon and seasonal interval coverage remains imperfect. Finally, multi-seed stability is limited to H30, and the training-budget sensitivity was evaluated at one representative station and horizon.

5. Conclusions

This study evaluated deterministic and calibrated probabilistic ET0 forecasting across seven stations in northern and southern Xinjiang using a complete rolling protocol. DLinear had the lowest regional RMSE at H30 and H180 in both northern and external groups and the lowest dense-grid CRPS under rolling calibration. H7 was station-dependent, with a small CNNBiLSTM advantage in the external group and a DLinear advantage in the northern core. H30 initialization stability also varied across sites, so the results support a conditional model-selection rule rather than one universally best model.

Probabilistic calibration improved average reliability and sharpness, but conditional coverage remained poor in spring and summer and failed the joint criteria at almost all H7 and H30 combinations. The 2024 field analysis further shows that generic soil and crop parameters do not reproduce observed root-zone moisture, so the irrigation results support a bounded sensitivity assessment rather than a field-calibrated recommendation. DLinear is a practical backbone under the tested protocol because it balances accuracy, probability quality and low inference cost, but external evaluation and site-specific soil-water calibration remain necessary before operational use.

Supplementary Materials: The following supporting information is available: Supplementary_Materials_Agriculture_Basel.xlsx, containing Tables S1-S19 (model settings, rolling metrics, seed stability, pairwise tests, probability diagnostics, data-quality audits and irrigation sensitivity analysis); Tables_Agriculture.xlsx, containing main Tables 1-6; and Figures 1-6 in 600-dpi PNG format.

Author Contributions: Conceptualization, D.C. and C.Y.; methodology, D.C.; software, D.C.; validation, D.C.; formal analysis, D.C.; investigation, D.C.; resources, C.Y.; data curation, D.C.; writing, original draft preparation, D.C.; writing, review and editing, C.Y.; visualization, D.C.; supervision, C.Y.; project administration, C.Y.; funding acquisition, C.Y. All authors have read and agreed to the published version of the manuscript.

Funding: This research was funded by the Xinjiang Uygur Autonomous Region Major Science and Technology Special Project, grant number 2022A02003-5. Chunfang Yue is the project leader.

Institutional Review Board Statement: Not applicable. This study used publicly available meteorological data and did not involve humans or animals.

Data Availability Statement: NOAA NCEI GSOD and NASA POWER data are publicly available from their respective archives. Processed station datasets, rolling forecasts, calibration outputs and analysis code are available from the corresponding author upon reasonable request. The water-user-level irrigation records are not publicly redistributed because they are operational records; aggregated irrigation-event tables are included in the Supplementary Materials.

Acknowledgments: During the preparation of this study, the authors used OpenAI Codex (Codex Desktop, 2026) + DeepSeek-V4.1-Flash to assist with code development, figure preparation, manuscript structuring and language editing. The authors reviewed and edited the output and take full responsibility for the content of this publication.

Conflicts of Interest: The authors declare no conflicts of interest. The funder had no role in the design of the study; in the collection, analysis or interpretation of data; in the writing of the manuscript; or in the decision to publish the results.

Abbreviations

Abbreviation	Definition
ET0	Reference evapotranspiration
FAO-56	FAO Irrigation and Drainage Paper 56
NCEI	National Centers for Environmental Information
GSOD	Global Summary of the Day
CRPS	Continuous ranked probability score
PICP	Prediction interval coverage probability
MPIW	Mean prediction interval width
RMSE	Root mean square error
NSE	Nash-Sutcliffe efficiency

References

1. Allen, R.G.; Pereira, L.S.; Raes, D.; Smith, M. Crop evapotranspiration—guidelines for computing crop water requirements. 1998.
2. Ippolito, M.; De Caro, D.; Cannarozzo, M.; Provenzano, G.; Ciraolo, G. Evaluation of daily crop reference evapotranspiration and sensitivity analysis of FAO penman-monteith equation using ERA5-land reanalysis database in sicily, italy. Agricultural Water Management 2024, 295, 108732. https://doi.org/10.1016/j.agwat.2024.108732
3. Chen, Z.; Zhu, Z.; Jiang, H.; Sun, S. Estimating daily reference evapotranspiration based on limited meteorological data using deep learning and classical machine learning methods. Journal of Hydrology 2020, 591, 125286. https://doi.org/10.1016/j.jhydrol.2020.125286
4. Bashir, R.N.; Mzoughi, O.; Shahid, M.A.; Alturki, N.; Saidani, O. Principal component analysis (PCA) and feature importance-based dimension reduction for reference evapotranspiration (ET0) predictions of taif, saudi arabia. Computers and Electronics in Agriculture 2024, 222, 109036. https://doi.org/10.1016/j.compag.2024.109036
5. Roy, D.K.; Sarkar, T.K.; Kamar, S.S.A.; Goswami, T.; Muktadir, M.A.; Al-Ghobari, H.M.; Alataway, A.; Dewidar, A.Z.; El-Shafei, A.A.; Mattar, M.A. Daily prediction and multi-step forward forecasting of reference evapotranspiration using LSTM and Bi-LSTM models. Agronomy 2022, 12(3), 594. https://doi.org/10.3390/agronomy12030594
6. Ferreira, L.B.; da Cunha, F.F.A. Multi-step ahead forecasting of daily reference evapotranspiration using deep learning. Computers and Electronics in Agriculture 2020, 178, 105728. https://doi.org/10.1016/j.compag.2020.105728
7. W. J. M. L. P. Jayasinghe; R. C. Deo; A. Ghahramani; S. Ghimire; N. Raj Deep multi-stage reference evapotranspiration forecasting model: multivariate empirical mode decomposition integrated with the boruta-random forest algorithm. IEEE Access 2021, 9, 166695-166708. https://doi.org/10.1109/ACCESS.2021.3135362
8. Karbasi, M.; Jamei, M.; Ali, M.; Malik, A.; Yaseen, Z.M. Forecasting weekly reference evapotranspiration using auto encoder decoder bidirectional LSTM model hybridized with a boruta-CatBoost input optimizer. Computers and Electronics in Agriculture 2022, 198, 107121. https://doi.org/10.1016/j.compag.2022.107121
9. Valipour, M.; Khoshkam, H.; Bateni, S.M.; Jun, C.; Band, S.S. Hybrid machine learning and deep learning models for multi-step-ahead daily reference evapotranspiration forecasting in different climate regions across the contiguous united states. Agricultural Water Management 2023, 283, 108311. https://doi.org/10.1016/j.agwat.2023.108311
10. Zhang, L.; Zhao, X.; Zhu, G.; He, J.; Chen, J.; Chen, Z.; Traore, S.; Liu, J.; Singh, V.P. Short-term daily reference evapotranspiration forecasting using temperature-based deep learning models in different climate zones in China. Agricultural Water Management 2023, 289, 108498. https://doi.org/10.1016/j.agwat.2023.108498
11. Granata, F.; Di Nunno, F.; de Marinis, G. Advanced evapotranspiration forecasting in central italy: stacked MLP-RF algorithm and correlated nystrom views with feature selection strategies. Computers and Electronics in Agriculture 2024, 220, 108887. https://doi.org/10.1016/j.compag.2024.108887
12. Ahmadi, A.; Daccache, A.; He, M.; Namadi, P.; Bafti, A.G.; Sandhu, P.; Bai, Z.; Snyder, R.L.; Kadir, T. Enhancing the accuracy and generalizability of reference evapotranspiration forecasting in california using deep global learning. Journal of Hydrology: Regional Studies 2025, 59, 102339. https://doi.org/10.1016/j.ejrh.2025.102339
13. Pan, J.; Yu, L.; Zhou, B.; Zhao, J. A daily reference crop evapotranspiration forecasting model based on improved informer. Agriculture 2025, 15(9), 933. https://doi.org/10.3390/agriculture15090933
14. Zhao, S.; Qiu, Y.; Yan, Z.; Wu, L.; Qiu, R.; Luo, Y. The potential of AI global weather models for reference evapotranspiration forecasting: a comparison with numerical weather prediction models. Journal of Hydrology 2026, 664, 134363. https://doi.org/10.1016/j.jhydrol.2025.134363
15. Karimi, S.; Sadeghzadeh, M.; Shiri, J.; Martí, P. Improving reference evapotranspiration estimation by attention-enhanced autoencoders and hybrid neural networks under noisy chaotic conditions. Journal of Hydrology 2026, 678, 136085. https://doi.org/10.1016/j.jhydrol.2026.136085
16. Li, Y.; Chen, W.; Hu, X.; Chen, B.; Sun, B.; Zhou, M. Transformer-modulated diffusion models for probabilistic multivariate time series forecasting. In Proceedings of the The Twelfth International Conference on Learning Representations (ICLR), 2024.
17. Pessoa, P.; Campitelli, P.; Shepherd, D.P.; Ozkan, S.B.; Pressé, S. Mamba time series forecasting with uncertainty quantification. Machine Learning: Science and Technology 2025, 6, 035012. https://doi.org/10.1088/2632-2153/adec3b
18. Zuo, L.; Zou, L.; Xia, J.; Zhang, L.; Cao, H.; She, D. Multi-scale analysis of six evapotranspiration products across china: accuracy, uncertainty and spatiotemporal pattern. Journal of Hydrology 2025, 650, 132516. https://doi.org/10.1016/j.jhydrol.2024.132516

19. Ju, X.; Chen, S. Evaluation and error attribution of evapotranspiration products over the haihe river basin: implications for irrigation scheduling and agricultural water management. Agricultural Water Management 2026, 329, 110358. https://doi.org/10.1016/j.agwat.2026.110358
20. Zhang, Y.; Yan, J. Crossformer: transformer utilizing cross-dimension dependency for multivariate time series forecasting. In Proceedings of the The Eleventh International Conference on Learning Representations (ICLR), 2023.
21. Liu, Y.; Hu, T.; Zhang, H.; Wu, H.; Wang, S.; Ma, L.; Long, M. iTransformer: inverted transformers are effective for time series forecasting. In Proceedings of the The Twelfth International Conference on Learning Representations (ICLR), 2024. https://openreview.net/forum?id=JePfAI8fah
22. Wang, S.; Wu, H.; Shi, X.; Hu, T.; Luo, H.; Ma, L.; Zhang, J.Y.; Zhou, J. TimeMixer: decomposable multiscale mixing for time series forecasting. In Proceedings of the The Twelfth International Conference on Learning Representations (ICLR), 2024. https://openreview.net/forum?id=7oLshfEIC2
23. Gu, A.; Dao, T. Mamba: linear-time sequence modeling with selective state spaces. In Proceedings of the First Conference on Language Modeling (COLM 2024), 2024.
24. Wang, Z.; Kong, F.; Feng, S.; Wang, M.; Yang, X.; Zhao, H.; Wang, D.; Zhang, Y. Is mamba effective for time series forecasting?. Neurocomputing 2025, 619, 129178. https://doi.org/10.1016/j.neucom.2024.129178
25. Zeng, A.; Chen, M.; Zhang, L.; Xu, Q. Are transformers effective for time series forecasting?. In Proceedings of the Proceedings of the AAAI conference on artificial intelligence, 2023, 11121-11128. https://doi.org/10.1609/aaai.v37i9.26317
26. Stitsyuk, A.; Choi, J. xPatch: dual-stream time series forecasting with exponential seasonal-trend decomposition. In Proceedings of the Proceedings of the AAAI Conference on Artificial Intelligence, 2025, 20601-20609. https://doi.org/10.1609/aaai.v39i19.34270
27. Nie, Y.; Nguyen, N.H.; Sinthong, P.; Kalagnanam, J. A time series is worth 64 words: long-term forecasting with transformers. In Proceedings of the The Eleventh International Conference on Learning Representations (ICLR), 2023.
28. Wu, Z.; Pan, S.; Long, G.; Jiang, J.; Chang, X.; Zhang, C. Connecting the dots: multivariate time series forecasting with graph neural networks. In Proceedings of the Proceedings of the 26th ACM SIGKDD International Conference on Knowledge Discovery & Data Mining, 2020, 753-763. https://doi.org/10.1145/3394486.3403118
29. Linker, R.; Sylaios, G. Efficient model-based sub-optimal irrigation scheduling using imperfect weather forecasts. Computers and Electronics in Agriculture 2016, 130, 118-127. https://doi.org/10.1016/j.compag.2016.10.004
30. Chen, X.; Qi, Z.; Gui, D.; Gu, Z.; Ma, L.; Zeng, F.; Li, L.; Sima, M.W. A model-based real-time decision support system for irrigation scheduling to improve water productivity. Agronomy 2019, 9(11), 686. https://doi.org/10.3390/agronomy9110686
31. Adeyemi, O.; Grove, I.; Peets, S.; Domun, Y.; Norton, T. Dynamic neural network modelling of soil moisture content for predictive irrigation scheduling. Sensors 2018, 18(10), 3408. https://doi.org/10.3390/s18103408
32. Domínguez-Niño, J.S.M.A.; Oliver-Manera, J.; Girona, J.; Casadesús, J. Differential irrigation scheduling by an automated algorithm of water balance tuned by capacitance-type soil moisture sensors. Agricultural Water Management 2020, 228, 105880. https://doi.org/10.1016/j.agwat.2019.105880
33. Yang, Y.; Hu, J.; Porter, D.; Marek, T.; Heflin, K.; Kong, H. Deep reinforcement learning-based irrigation scheduling. Transactions of the ASABE 2020, 63(3), 549-556. https://doi.org/10.13031/trans.13633
34. Pereira, L.S.; Paredes, P.; Jovanovic, N. Soil water balance models for determining crop water and irrigation requirements and irrigation scheduling focusing on the FAO56 method and the dual kc approach. Agricultural Water Management 2020, 241, 106357. https://doi.org/10.1016/j.agwat.2020.106357